Research article

Yaxin Zhang[a], Yuncheng Zhao[a], Shixiong Liang, Bo Zhang*, Lan Wang, Tianchi Zhou, Wei Kou, Feng Lan, Hongxin Zeng, Jiaguang Han, Zhihong Feng, Qin Chen, Pinaki Mazumder and Ziqiang Yang

Large phase modulation of THz wave via an enhanced resonant active HEMT metasurface

https://doi.org/10.1515/nanoph-2018-0116
Received August 7, 2018; revised October 27, 2018; accepted November 1, 2018

Abstract: Terahertz (THz) science and technology promise unique applications in high-speed communications, high-accuracy imaging, and so on. To keep up with the demand for THz systems, THz dynamic devices should feature large phase shift modulation and high speed. To date, however, only a few devices can efficiently manipulate the phase of THz waves. In this paper, we demonstrate that efficient phase modulation of THz waves can be addressed by an active and enhanced resonant metamaterial embedded with a nanostructured 2D electron gas (2DEG) layer of a GaN high electron mobility transistor (HEMT). The enhanced resonant metaunit couples the traditional dipolar and inductance-capacitance resonances together to realize a coupling mode with enhanced resonance. Embedded with the nanostructured 2DEG layer of GaN HEMT, the resonance intensity and surface current circuit of the enhanced resonant mode in the metamaterial unit can be dynamically manipulated by the electrical control of the carrier distribution and depletion of the 3 nm 2DEG, leading to a phase shift greater than 150° in simulation. In the dynamic experiments, a 137° phase shift was achieved with an external controlling voltage of only several volts in the THz transmission mode. This work represents the first realization of a phase shift greater than 100° in a dynamic experiment in transmission mode using an active metamaterial structure with only a single layer. In addition, given the high-speed modulation ability of the HEMT, this concept provides a promising approach for the development of a fast and effective phase modulator in THz application systems.

Keywords: coupling mode; 2-DEG; meta-surface; phase shift; terahertz; GaN HEMT.

1 Introduction

As a notable and attractive area of scientific research, the field of terahertz (THz) science and technology has developed rapidly in the past decades. Because of their potential applications in security checking, wireless communications, and imaging, THz application systems have attracted much interest [1–11]. To use THz waves for data transmission in communication and imaging, the effective manipulation of the amplitude and phase of THz waves has been highly demanded and has become a subject of intense research. Starting with the earliest work in 2006 on combining metamaterials and doped semiconductors

[a]Yaxin Zhang and Yuncheng Zhao are co-first authors.
***Corresponding author: Bo Zhang,** Terahertz Science Cooperative Innovation Center, School of Electronic Science and Engineering, University of Electronic Science and Technology of China, Chengdu, China, e-mail: bozhang@uestc.edu.cn
Yaxin Zhang: Terahertz Science Cooperative Innovation Center, School of Electronic Science and Engineering, University of Electronic Science and Technology of China, Chengdu, China; and National Key Laboratory of Application Specific Integrated Circuit, Hebei Semiconductor Research Institute, Shijiazhuang, China
Yuncheng Zhao, Lan Wang, Tianchi Zhou, Wei Kou, Hongxin Zeng, Qin Chen and Ziqiang Yang: Terahertz Science Cooperative Innovation Center, School of Electronic Science and Engineering, University of Electronic Science and Technology of China, Chengdu, China. https://orcid.org/0000-0002-9511-9789 (Y. Zhao)
Shixiong Liang and Zhihong Feng: National Key Laboratory of Application Specific Integrated Circuit, Hebei Semiconductor Research Institute, Shijiazhuang, China
Feng Lan: Terahertz Science Cooperative Innovation Center, School of Electronic Science and Engineering, University of Electronic Science and Technology of China, Chengdu, China; and Department of Electrical Engineering and Computer Science, University of Michigan, Ann Arbor, MI, USA
Jiaguang Han: Center for Terahertz Waves and College of Precision Instrument and Optoelectronics Engineering, Tianjin University, Tianjin, China
Pinaki Mazumder: Department of Electrical Engineering and Computer Science, University of Michigan, Ann Arbor, MI, USA

to realize amplitude modulation of THz waves [12], intense effort has been devoted in the area of active THz metamaterials to develop ultrafast THz dynamic devices [13–29]. The integration of doped silicon [13–15], GaAs semiconductor material [16], high electron mobility transistors (HEMTs) [17], VO_2 phase transition material [18–21], and graphene with metamaterials [22–33] has been applied to enable the optical and electrical control of THz wave transmission. However, most of these previous works focused on the amplitude modulation of THz waves to develop THz switches, THz modulators for on-off keying communication, and wavefront-coding imaging devices, whereas relatively few researchers have attempted to achieve THz phase modulation using semiconductor-metamaterial structures [16, 34–37].

The phase control of THz waves, particularly in the transmission state, is well known to be important for THz wireless communication with phase shift keying modulation and for THz imaging systems; therefore, the development of a phase modulator with a 360° phase shift is both important and urgent. A phase-control THz metamaterial based on an n-doped GaAs layer was recently reported [16]. This device realized 0.56 rad phase modulation by transmission mode. Following this work, several authors reported related experimental work on THz phase modulators. The epitaxial stacking of multiple phase modulation layers may provide an approach for achieving a 360° shift; however, the loss rises dramatically with an increasing number of layers. Thus, a single-layer structure that can realize a phase shift larger than 120° is critical for the development of a 360° THz phase modulator.

The recent rapid development of 2D electron gas (2DEG) devices provides a promising approach for the development of dynamic THz devices [37–40]. In the AlGaN/GaN heterostructure interface, the formation of a nanoscale 2DEG layer with a high concentration and a high mobility can be induced by the spontaneous polarization effect and the piezoelectric polarization effect. Therefore, in the present work, an enhanced resonant metamaterial embedded with a nanostructured 2DEG layer of GaN HEMT is proposed to address the efficient phase modulation of THz waves.

2 Device design and fabrication

The unit cell of the active metasurface, as depicted in Figure 1, comprises three layers: (i) SiC substrates, (ii) an AlGaN/GaN heterostructure, and (iii) an enhanced resonant metamaterial embedded with a nanostructured 2DEG layer.

In this structural system, the heterostructure of GaN HEMT consists of a 25-nm-thick $Al_{0.27}Ga_{0.73}N$ barrier layer, a 1 μm undoped GaN layer, and a 1.5 μm GaN buffer layer. In this AlGaN/GaN heterostructure, a channel between the AlGaN and GaN layers provides approximately 3-nm-thick 2DEG layers with a sheet carrier concentration of 9.2×10^{12} cm^{-2} and an electron mobility of 2170 cm/(V s) at room temperature, corresponding to a sheet resistance of 280 Ω/□. The 2DEG nanostructures, which can be placed in some strategic regions of the metamaterial unit, as shown in the red region in Figure 1A, are considered the key tunable element for the modulation of the THz transmission properties of the composite metamaterial structure. For the metamaterial layer, one unit cell consists mainly of a circular split-ring resonator (CSRR), a perpendicular long wire dipolar resonator, and a long parallel grid wire. The nanostructured 2DEG is embedded in the geometric center of the gap of the CSRR connecting the two plates of the unit. Each plate integrated with 2DEG by ohmic contact constitutes the source and drain electrodes. The center long

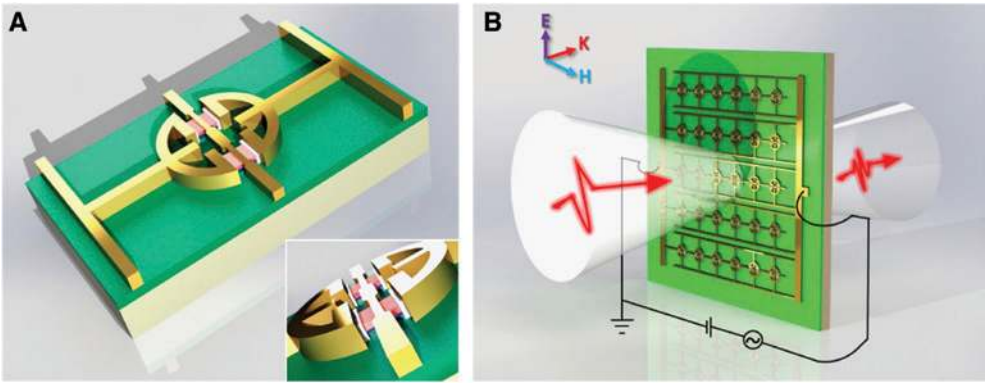

Figure 1: Structures of the enhanced resonant metamaterial embedded with nanostructured 2DEG layer: (A) 3D structure of a unit cell and (B) schematic of the phase modulator.

wire connected to 2DEG by a Schottky contact with a gate length of 1 μm acts as the electrical control grid. Therefore, the plates of the metamaterial, together with the Schottky gate and the 2DEG of the GaN heterostructure, constitute a grid-control active metamaterial unit. The electromagnetic properties, and therefore the effective resonant characteristics of the metamaterial unit, can be adjusted via electrically controlling the distribution of the carriers of the 2DEG nanostructure to modulate the phase of the perpendicular incident THz waves (Figure 1B).

As shown in Figure 2, a series of chemical and physical methods, mainly containing six steps, were used to fabricate the device.

First, the AlGaN(25 nm)/GaN(1.5 μm) heterostructure film was grown on a 160 μm SiC substrate by metal-organic chemical vapor deposition. Next, a 1.5-μm-thick positive photoresist layer was spin coated on top of the AlGaN film. After the standard photolithography process, the photoresist layer functioned as a mask to define the active region of 2DEG and the AlGaN film outside the active region was overetched by inductively coupled plasma of hybrid Cl_2-BCl_3. Through the above excessive etching process, hathpace-like active regions (35-nm-thick 2DEG nanostructure) can be obtained. The AlGaN layer in other area (except active regions) is disappeared. Through photoetching, electron-beam evaporation, and lift-off processes, a complex metal layer of Ti/Al/Ni/Au (20/120/70/100 nm) was orderly deposited onto both ends of the active regions as source and drain electrodes. After a rapid annealing process at 900°C under an N_2 environment, just as the temperature drops rapidly from 900°C to 25°C in 140 s, the source and drain electrodes form ohmic contact with the 2DEG. Following similar photoetching, electron-beam evaporation and lift-off processes, the metamaterial structure, a 200 nm gold layer with a 50 nm nickel adhesion layer was deposited onto the GaN layer. Specially, the branches of the ring-shaped metamaterial structure cover the source and drain electrodes. Thus, the metamaterial structure and the 2DEG nanostructure form ohm contact through the source and drain electrodes. At last, the gate Au/Ni (150/50 nm) was fabricated by accurate electron-beam lithography.

The fabricated structure and packaged devices are shown in Figure 3. The coplanar waveguide (CPW) has been

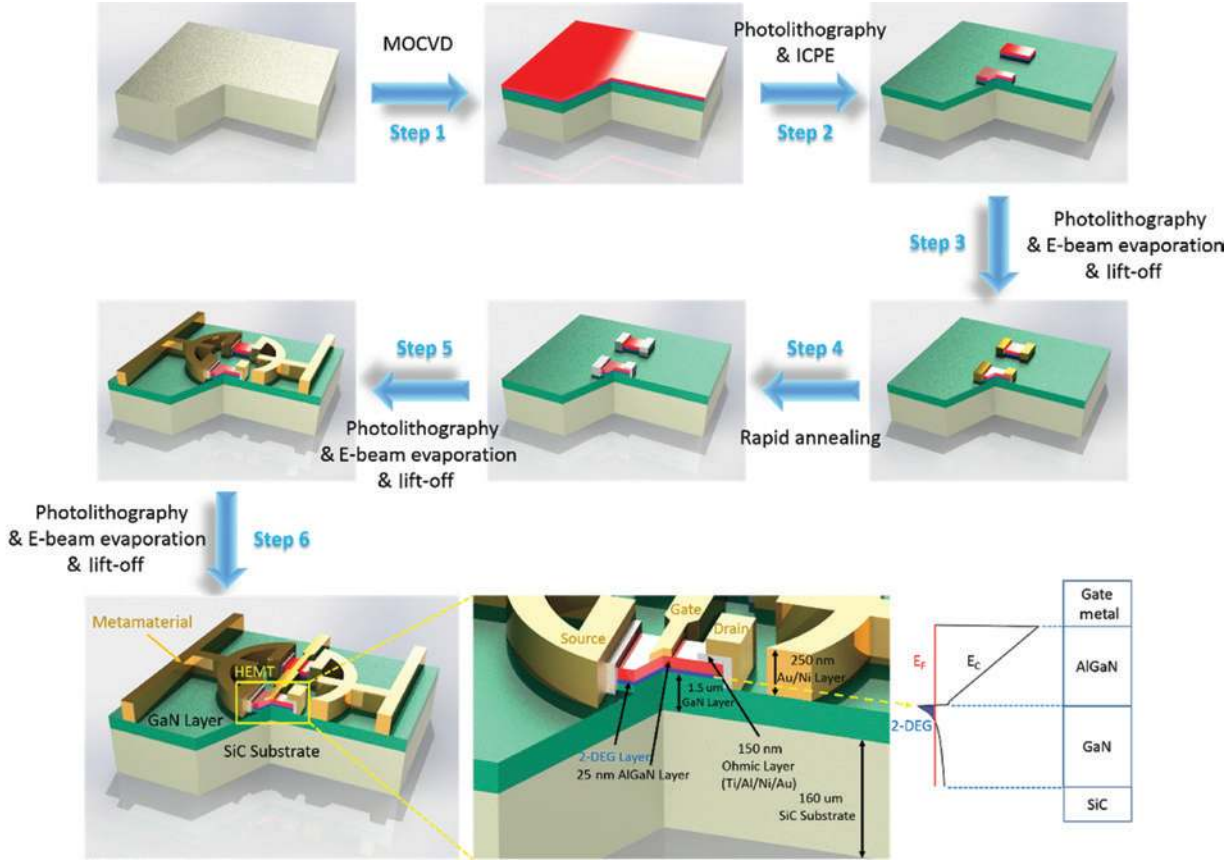

Figure 2: Process flow for the fabrication of enhanced resonant metamaterial embedded with the nanostructured 2DEG layer.

applied to input the voltage signal as shown in Figure 3A. The CPW (Figure 3D) in the chip is matched to the CPW in the printed circuit board (PCB). Gold wire has been used to bond the CPWs in PCB and chip as shown in Figure 3B and C. The amplified array is depicted in Figure 3E.

3 Results and discussion

3.1 Analysis of the relation between phase jump change and resonance

First, the large phase modulation mechanism was investigated. From a previous work, we know that, according to the Kramers-Kronig (KK) relation, the transmission amplitude and phase through a structured surface are not independent of each other [41]. The KK relation shows that no phase modulation occurs near the frequency where the maximum amplitude modulation is obtained. In contrast, the maximum phase shift corresponds to the minimum amplitude change. Moreover, according to the KK relation, a phase jump change always occurs around a transmission resonant peak as demonstrated in the literature [16, 42]. Therefore, to achieve a large phase shift, a large phase jump change should first be induced in a metamaterial unit cell. By deducing the KK relation (detailed derivation shown in Appendix F), it demonstrates that the phase is directly related to $\mathrm{d}\ln|G|/\mathrm{d}\ln|\omega|$ ($|G|$ is the amplitude of the electromagnetic wave). Therefore, to get the large phase jump by the induced resonant mode of the metaunit, first, we have to achieve the large value of $\mathrm{d}\ln|G|/\mathrm{d}\ln|\omega|$. Therefore, the relation between the resonance intensity and the phase jump change was investigated.

Various resonant modes with different resonance intensities, such as inductance-capacitance (LC) resonance [12–17], dipole resonance (DR) [37], and Fano resonance (FR) [43–46], among others [47–56], have been realized through the careful design of the electromagnetic structures of metamaterials. Therefore, to extract persuasive information regarding the characteristics of different

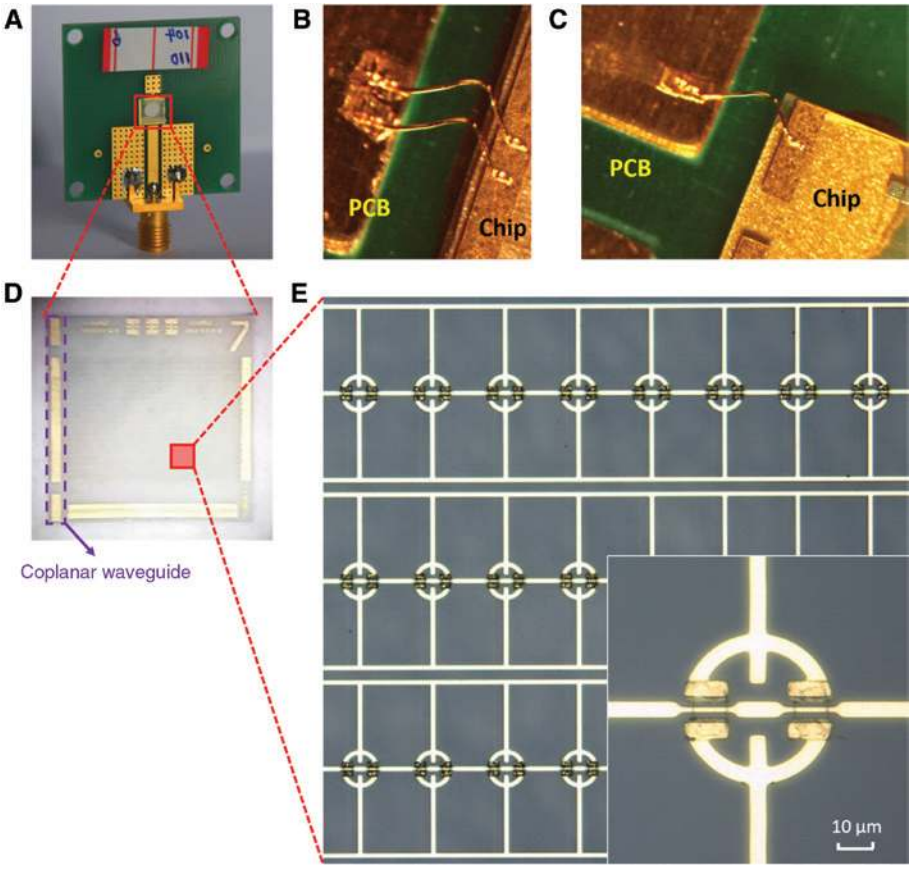

Figure 3: Manufactured sample: (A) image of a packaged phase modulator, (B and C) gold bonding wires connecting the CPWs (PCB and chip), (D) image of the chip, and (E) photomicrograph of a portion of the fabricated structure.

resonances, we compared three representative resonance structures: LC, dipole, and Fano metamaterials. Next, the transmission and phase jump change as functions of the frequency of these representative metamaterials were numerically studied using the commercial 3D fully electromagnetic simulation software CST Microwave Studio; the results are shown in Figure 4 (details of the sizes of the structures shown in Appendix A). The simulation results for the transmission rate and phase were directly obtained from the CST software. The transmission was defined as $20\log_{10}(E_{out}E_{in})$, where E_{in} is the electric intensity of the incident THz wave and E_{out} is the transmitted electric intensity. In the phase calculation, the phase of the substrate was used as the reference.

In Figure 4, several structures corresponding to different resonances are depicted. The first one is the FR of an asymmetrical structure (Figure 4A). The second is the LC resonance of a split-ring resonator (SRR; Figure 4B). The third one is the DR of a circular ring (Figure 4C). The coupled metamaterial unit cell that combines an LC resonance structure and a DR structure, as shown in the last structure (LCDR) depicted in Figure 4D, is proposed. The transmission rates and phase shift of these resonances are shown in Figure 4E.

The current distribution of the induced LC resonance clearly shows that the current flows as a circuit loop in the unit (Figure 4B). The surface current of the DR flows along a direction in the metal wires (Figure 4C). In this

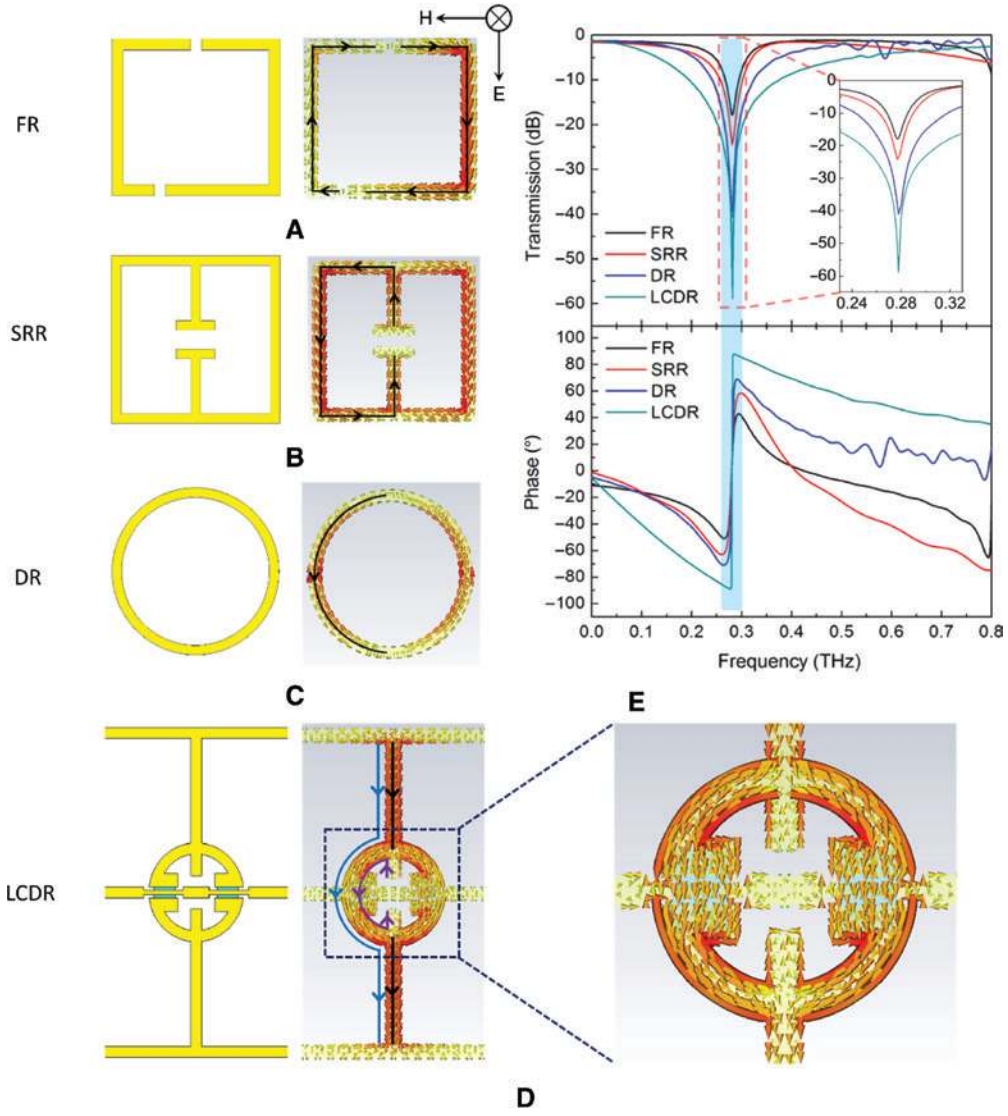

Figure 4: Simulation results of different resonance structures: (A) FR structure with current distribution, (B) LC resonance structure with current distribution, (C) DR structure with current distribution, (D) coupled resonance structure with current distribution, and (E) transmission and phase spectra for different structures.

LCDR resonance structure, the LC resonance couples with the DR so that the electromagnetic characteristics of LCDR integrate those of both LC and DR. Therefore, the surface current flows in two paths. The first path is shown by the blue arrow that depicts the current flowing from the upper metal wire to the lower wire across the outer edge of the center circular split ring, which is similar to the distribution of the DR. The second path is shown by the purple arrow, which shows the current flowing in a loop along the inner edge of the center circular split ring. This distribution is the same as that of the LC resonance. Therefore, we refer to this mode as the LCDR mode.

Moreover, for the DR, the field intensity is concentrated on both sides of the metal wire of the unit. In the LC resonance, the field intensity is focused in the center split gap of the unit. In the present LCDR resonance, we find that the field oscillates not only along the long wires but also in the center circular split ring such that the field intensity is concentrated in both sides and in the center of the unit (Figure 5A). Therefore, around the resonant frequency peak, more energy from the incident wave is trapped and is resonant in the unit. The absorptive resonant intensity is larger as shown in Figure 4E by the green solid line corresponding to this mode.

More importantly, the phase-frequency curve as shown in Figure 4E illustrates that, around the frequency peak, there is a sudden phase jump that could be explained by the KK relation as mentioned above. By comparing the two graphs of Figure 4E, the value of the phase jump change was found to be closely related to the resonant intensity. A comparison of the results reveals an important relation: the stronger resonant intensity corresponds to a larger phase jump change around the resonant frequency. This conclusion is also according with the KK relation derivation that the strong resonant intensity leads to a large value of $\mathrm{d}\ln|G|/\mathrm{d}\ln|\omega|$, which is directly related to the value of the phase (detailed derivation shown in Appendix F). Therefore, because of the enhanced resonant intensity, the phase jump change of the LCDR can reach 178°, which is much larger than those for the other, traditional resonances. Therefore, this structure is an ideal metaunit that could lead to a large phase modulation of THz waves.

3.2 Analysis of dynamic mode conversion controlled by the 2DEG nanostructure

Based on the study of the relation between the resonant intensity and phase jump, considering the role of 2DEG of GaN HEMT, the dynamic physical process of phase modulation of THz waves has been studied. In the analysis, we applied the Drude model (details shown in Appendix D)

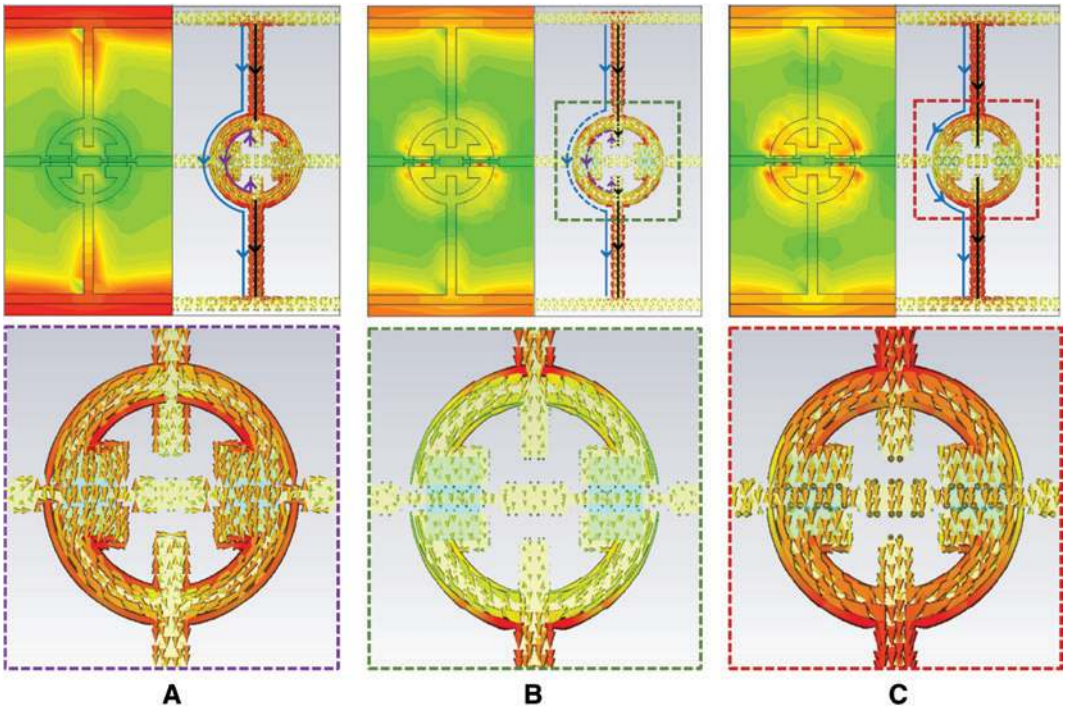

Figure 5: Simulation results of the electric field distribution and current density with different carrier density: (A) carrier density = 2×10^{12} cm^{-2}, (B) current density = 2×10^{10} cm^{-2}, and (C) carrier density = 2×10^{5} cm^{-2}.

equivalent to the characteristics of a 2DEG. Given that the 2DEG nanostructure with 3 nm depth is embedded with such an enhanced resonant metamaterial, the change of carrier distribution and the depletion of 2DEG could lead to resonant mode conversion of the metaunit as shown in Figure 5.

Further analyses of the surface current distribution and the electrical field contour map of the coupling mode in the unit cell were carried out with different carrier densities of the 2DEG nanostructure. In the original state, no external voltage is loaded on the grid in the center. Because of the high carrier density of the 2DEG nanostructure, the plates of the center gap of the unit cell are connected to each other by such a 2DEG. As depicted in Figure 5A, the incident THz wave induced a coupling mode for which the inner circuit is just a typical LC loop and the outer circuit is the dipolar loop as mentioned above in the LCDR structure. Furthermore, when the external voltage was loaded on the grid of the unit, the carrier in the 2DEG nanostructure was rearranged and depleted gradually while the source and drain plates were separated to reconfigure the unit cell structure. As shown in Figure 5B, with the depletion, the mode was gradually converted. In the case of a very low carrier density, the induced resonant mode of the metaunit differed substantially from that in the original state. An examination of Figure 5C shows that, when the carrier density is only 2×10^5 cm^{-2}, the surface current flows through the long wire and splits by two quarters of a circle, which is another coupling mode between the DR in the CSRR and the long wire. As a result, such mode conversion leads to a large phase shift. This process can also be observed in the transmission diagram shown in Figure 6. The simulations are respectively performed by CST Microwave Studio with transient solver and frequency-domain solver. For the single unit (simulated by transient solver with standard electromagnetic boundary), in the original state, the resonant frequency is approximately 0.3 THz with −61 dB resonance; as 2DEG is depleted, the resonance intensity decreases and the phase shift jump change becomes smaller. When the carrier density separating the drain and source plates is sufficiently small, the resonant mode gradually changes and the resonance frequency blueshifts to 0.42 THz step by step as shown in Figure 6. Finally, when the carrier density is less than 10^{-8} cm^{-2}, the enhanced resonant mode with −68 dB resonance intensity is achieved. Therefore, because of the mode conversion, enhanced resonance blueshift leads to a greater than 150° phase shift in the simulation from 0.33 to 0.39 THz as shown in the red area in Figure 6; to the best of our knowledge, a phase shift of this magnitude has never been reported even in simulations of a one-layer metamaterial structure. Moreover, to be more realistic, a frequency-domain solver using periodic boundary condition (array) is carried out to study the collective effect among the units. It shows that, considering the mutual influence of each unit, the frequency peak shifts slightly and the resonant intensity decreases a bit.

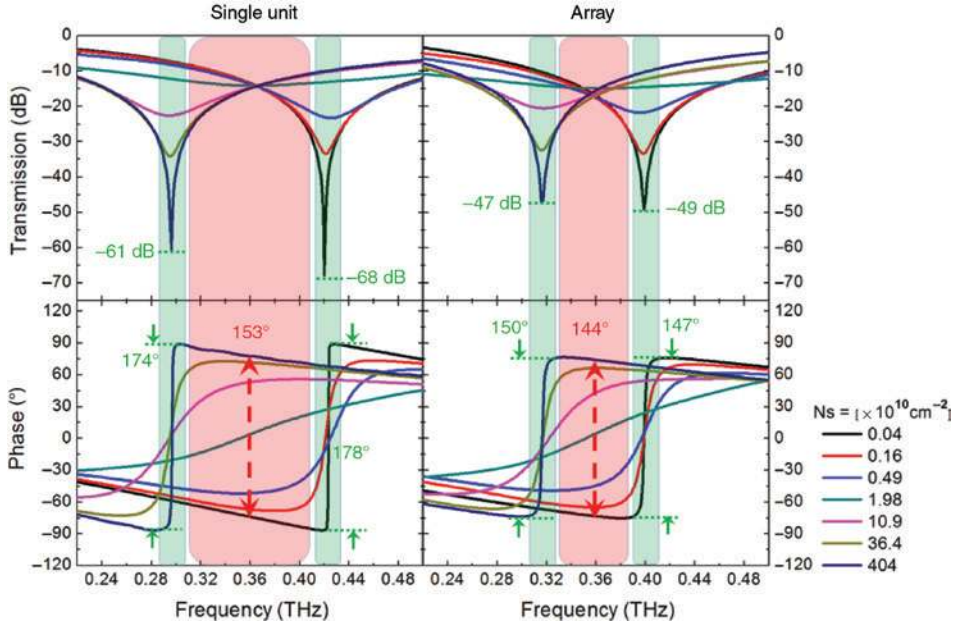

Figure 6: Simulation results of the transmission and phase spectra with different carrier densities for single unit and an array.

Constructing an equivalent circuit model contributes to analyze and verify the above-mentioned conversion between different surface current distributions [57]. The equivalent circuit model for the LCDR structure is shown in Figure 7A. First of all, the LCDR structure can be divided into three kinds of parallel circuits. Each circuit corresponds to different RLC parameters. As this structure is bilateral symmetry, we only analyze half of this unit. The first circuit is shown as the blue path in Figure 5A; the incident wave can induce the dipole-like resonance along this route, so it can be expressed by L_{31}, R_{31}, and C_{31} just as shown in both sides of the circuit model. The second circuit is shown as the purple line in Figure 5A; this route is just corresponding to the LC-like resonance so that the circuit is composed of the L_{21}, R_{21}, C_{23}, and R_{23} parameters. Moreover, it should be noted that in the gap there is the 2DEG region; thus, we should consider the parallel capacitance C_0 shown in the model. The last circuit (black line in Figure 5A) is the center vertical long wire and this dipole-like resonance is equal to L_1 and C_1. According to the formula $T(\omega)=2/(2+jZ_{in})$, where Z_{in} is the input impedance of circuit, the transmission $[T(\omega)]$ can be calculated. The detailed derivation and the value of the parameters in equivalent circuit are shown in Appendix E.

The simulation results of this equivalent circuit obtained from Advanced Design System (ADS) software are shown in Figure 7B (dashed lines). The progress that the resistances (R_{21}, R_{22}, R_{23}, and R_{31}) decrease gradually from 1900 to 0.001 Ω corresponds to the increase of 2DEG carrier concentration N_S from 4×10^8 to 4.04×10^{14} cm^{-2}. Obviously, the simulation results of 3D electromagnetic model and equivalent circuit model are very consistent.

3.3 Analysis of dynamic experiment

To characterize the phase modulation performance of this device, THz time-domain spectroscopy (THz-TDS) using the Teraview TPS3000 spectrometer (details provided in Appendix B) in transmission mode was conducted. In the experiments, a normal incident THz wave is perpendicularly projected onto the surface of the phase modulator with the polarization of the electric fields parallel to the split gaps and a direct current voltage is applied to the device shown in Figure 1B.

The original time-domain signals and the phase shift with different voltages are shown in Figure 8; similar to the simulation results, the external voltage could control the resonant characteristics to adjust the phase shift. By adjusting the voltage loaded on the grid due to the distribution of internal electric field change in the HEMT, the carrier density of the 2DEG nanostructure was adjusted correspondingly. With increasing voltage, the carrier density of the 2DEG nanostructure was gradually decreased and depleted, resulting in mode conversion in the unit cell. Therefore, the phase jump change was controlled via the voltage alternation as shown in Figure 8B and C. The agreement between the experimental results and those of the simulation demonstrates that the distribution and density change of carriers of the 2DEG nanostructure led to the reconfiguration of the metamaterial unit

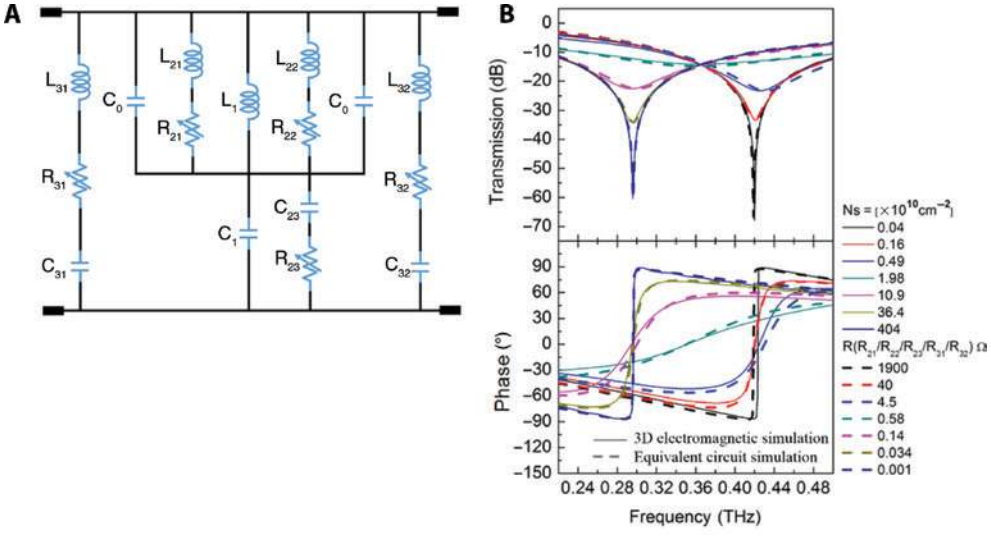

Figure 7: (A) Equivalent circuit model for LCDR and (B) 3D electromagnetic (continuous lines) and equivalent circuit (dashed lines) simulation for dynamic modulation processes.

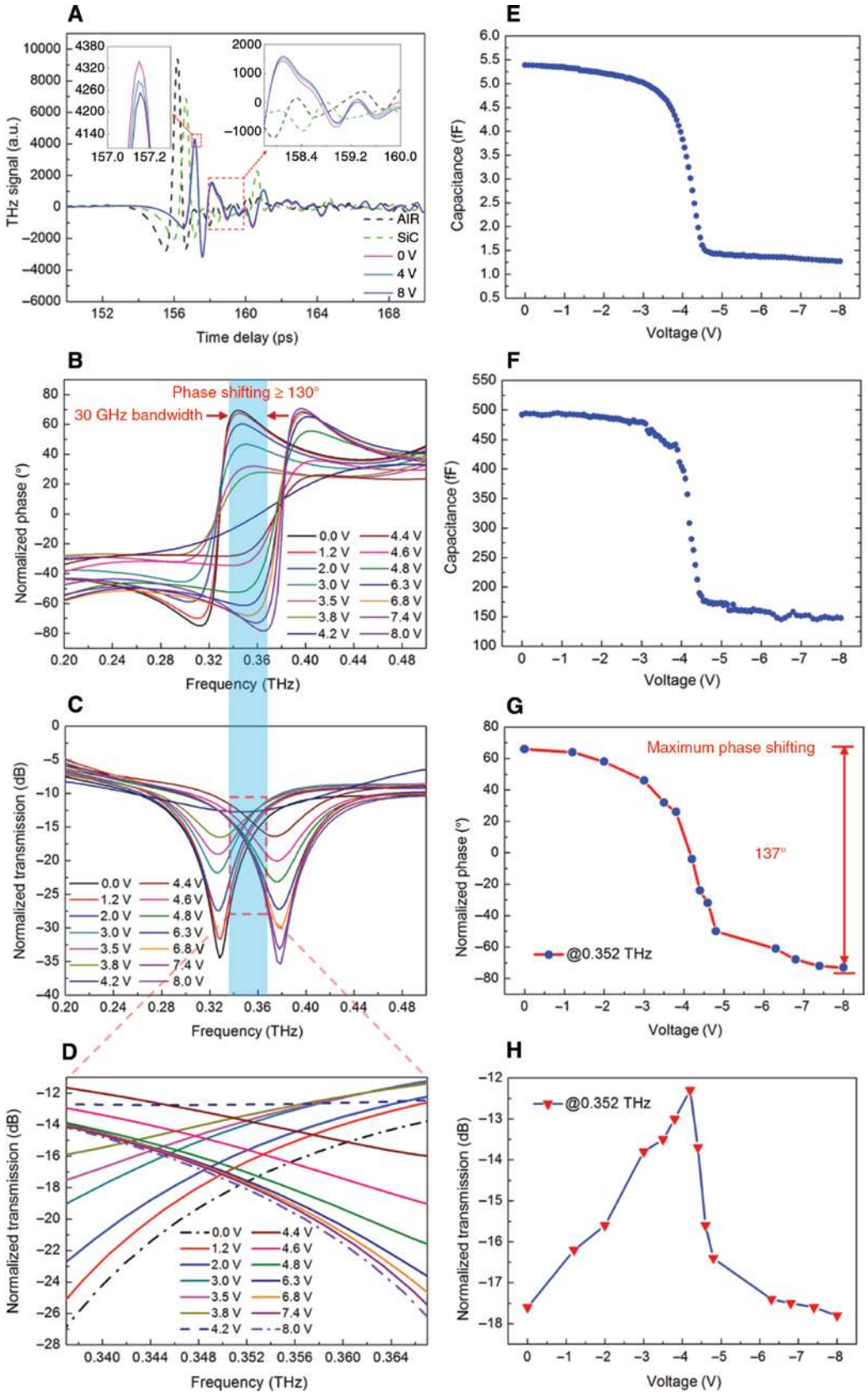

Figure 8: THz experimental results with the variation of voltages: (A) original time-domain data of TDS with different voltages, (B) phase shift with different voltages, (C) transmission spectrum with different voltages, (D) transmission spectrum in working band, (E) C-V relation of a single HEMT, (F) C-V relation of an array, (G) phase shift at 0.352 THz with different voltages, and (H) transmission at 0.352 THz with different voltages.

cell, inducing the coupling mode conversion. Such mode conversion results in a shift of the phase jump frequency such that a large phase shift is achieved. Excitingly, Figure 8B shows that, at frequencies of approximately 0.352 THz, the largest phase shift approaches 137°, and in the working band (0.337–0.367 THz) of this device, the phase shift can be more than 130°. As shown in Figure 8D, the amplitude transmission also increases first and then decreases in working band. The maximum amplitude loss is about –27 dB and the minimum loss at the central frequency point is about –18 dB. As shown in Figure 8H, as the voltage increases, the transmission loss decreases first (from –17.7 to –12.7 dB) and then increases (from –12.7 to –17.8 dB) at a center working frequency of 0.352 THz. Therefore, where the phase shift is greatest, the amplitude loss is relatively minimal, which is beneficial to the phase modulator. More importantly, the C-V relation of a single HEMT and an array has been tested independently as shown in Figure 8E and F by a probe station as shown in Appendix C. By comparing to the phase curve depending on the frequency shown in Figure 8G, it is clear that the physics laws of these three figures are nearly the same, which shows that the consistency of this optimized device is very good. Moreover, it also illustrates that the characteristics of the dynamic phase shift are determined by the C-V relation of the HEMT.

Furthermore, by comparing the experimental results in Figure 8B and C and the simulation results of the array in Figure 6, the experimental results agree well with the simulation. However, there are some minor discrepancies that may be caused by the mismachining tolerance, dielectric parameter difference between the simulation and realistic results, and the method that applies the Drude model to represent the change in the external voltage.

Nonetheless, this large phase shift with a single-layer active metamaterial structure in transmission mode is still very attractive and verifies that such a combination of a mode-coupling metamaterial and the 2DEG nanostructure of GaN HEMT is an effective approach for the realization of a large phase shift. In view of the high electron mobility of 2DEG, this phase modulator should have an ultrafast modulation speed. In addition, the active region (2DEG nanostructure) is very small (only 12×8 μm), which makes external voltage loading more efficient and reduces parasites. This design is helping to improve the modulation speed. According to the method presented in Ref. [22], the expected modulation speed of this phase modulator could be evaluated from the inverse of the calculated RC time constant. R and C are the resistance and capacitance, respectively. RC time constant is the product of R and C.

The inverse value of the capacitance and resistance of the array structure in the modulator are 0.33 pF (according to Figure 8F) and 1.270 Ω, respectively, which are averaged over a voltage sweep of 0 to –8 V. Therefore, based on the expression mentioned above, the calculated RC time constant corresponds to about 2.4 GHz modulation speed.

4 Conclusion

An enhanced resonant metamaterial embedded with a nanostructured 2DEG layer of GaN HEMT was proposed and experimentally demonstrated to achieve a large phase modulation of THz waves. Because the resonant intensity of the induced mode in a metasurface was found to be closely related to a phase jump change, the presented metamaterial could lead to a much larger phase jump change than the traditional metasurface structure. More importantly, by electrically tuning the distribution and density of the carrier of the 2DEG nanostructure, the conversion between two different coupling modes of this metamaterial surface could be controlled. Such mode conversion led to a large phase modulation of THz waves. The dynamic experimental results showed that a 137° phase shift was achieved at approximately 0.35 THz with the application of 0 to 8 V for the electrical control of the THz transmission mode. Moreover, using the method of a phase shifter in a microwave regime, by cascading three layers based on this device, the 2π phase shifter might be achieved. Meanwhile, given the mobility of 2DEG in the GaN HEMT, the fast modulation of the phase of the transmitted THz waves was realized.

Appendix A: Details of the simulation with different resonance structures

To extract persuasive information regarding the characteristics of different resonances, the studies were performed by comparing three representative resonance structures: the LC, dipole, and Fano metamaterials. The compared figure is shown in Figure 4.

In the simulation, SiC is the substrate material for different metamaterial structures. The dielectric constant of substrate is set as 9.8 and the thickness is 160 μm. The detail parameters of the four metaunits are shown in Appendix-Figures 1–4. The geometrical features of these different structures have been swept to obtain the

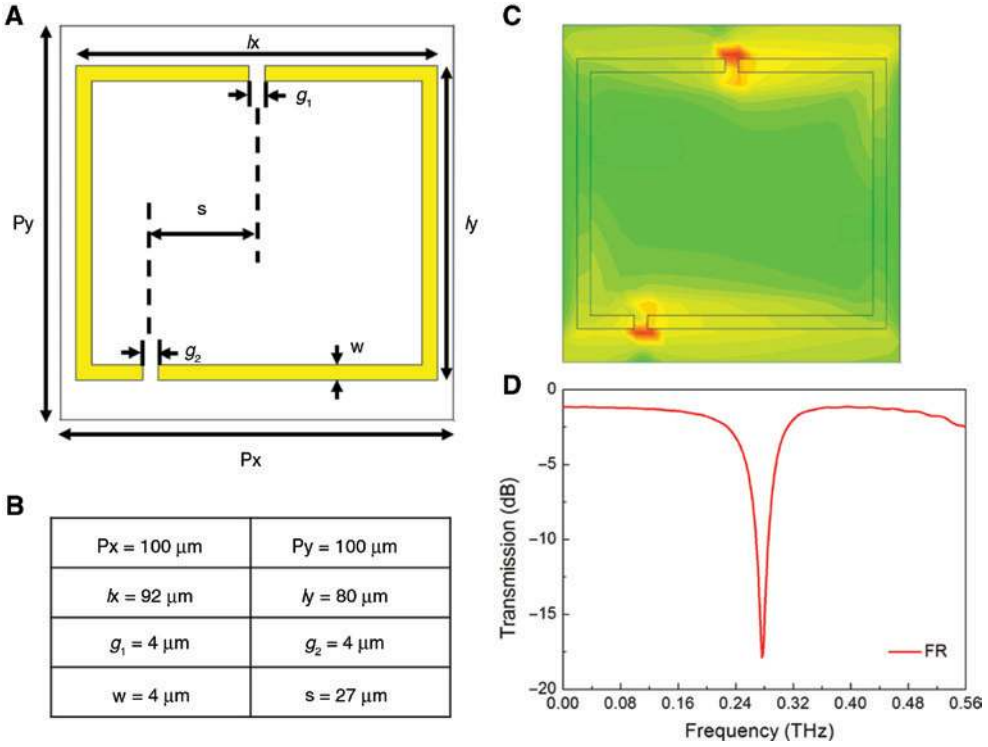

Px = 100 μm	Py = 100 μm
lx = 92 μm	ly = 80 μm
g_1 = 4 μm	g_2 = 4 μm
w = 4 μm	s = 27 μm

Appendix-Figure 1: Simulation detail of FR: (A) 2D structure model, (B) structural parameters, (C) electrical field distribution, and (D) transmission spectrum.

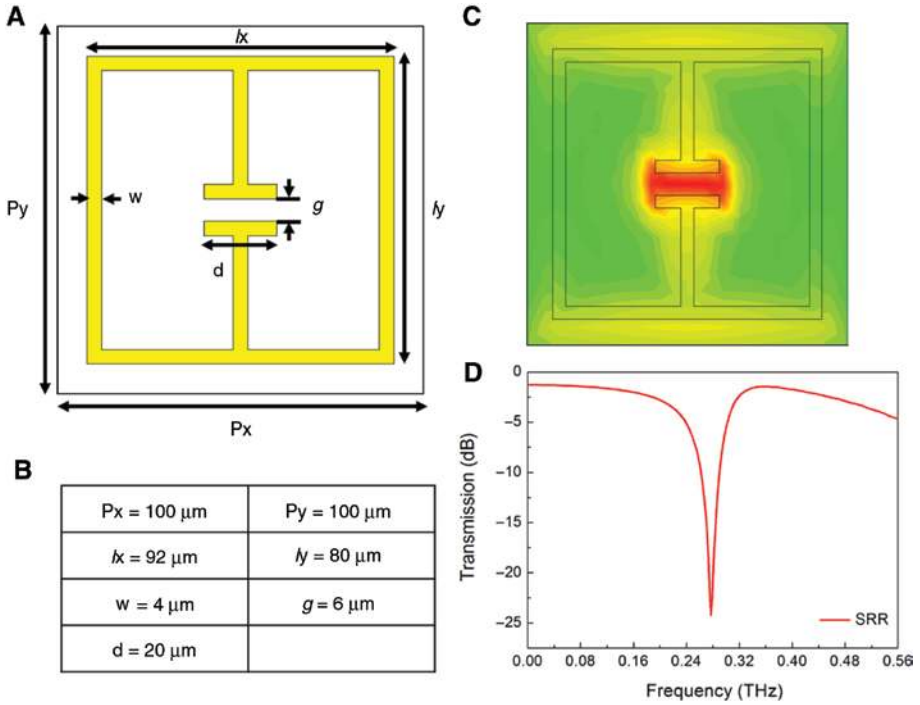

Px = 100 μm	Py = 100 μm
lx = 92 μm	ly = 80 μm
w = 4 μm	g = 6 μm
d = 20 μm	

Appendix-Figure 2: Simulation detail of SRR: (A) 2D structure model, (B) structural parameters, (C) electrical field distribution, and (D) transmission spectrum.

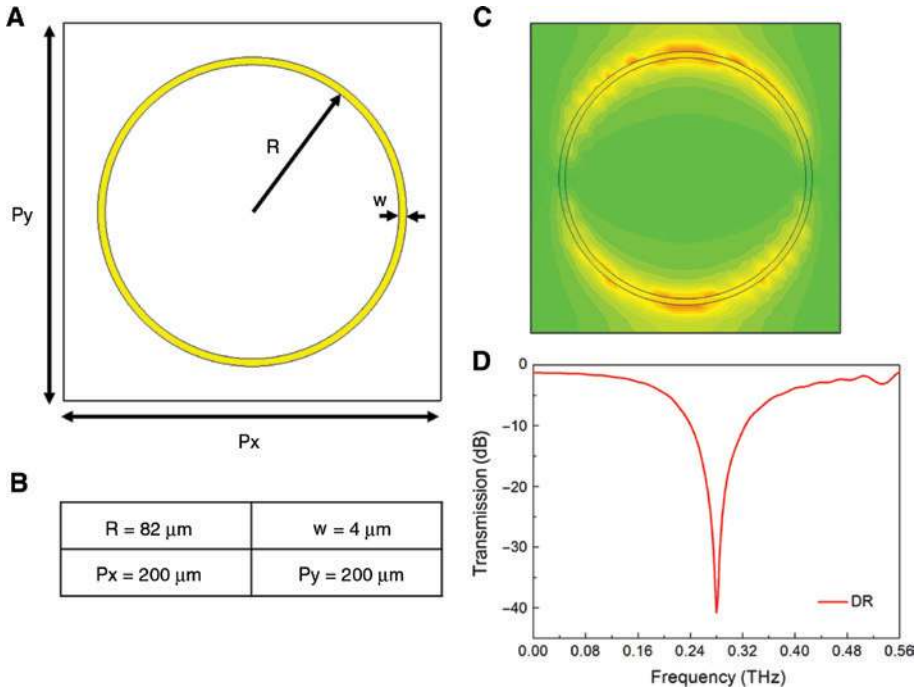

R = 82 μm	w = 4 μm
Px = 200 μm	Py = 200 μm

Appendix-Figure 3: Simulation detail of DR: (A) 2D structure model, (B) structural parameters, (C) electrical field distribution, and (D) transmission spectrum.

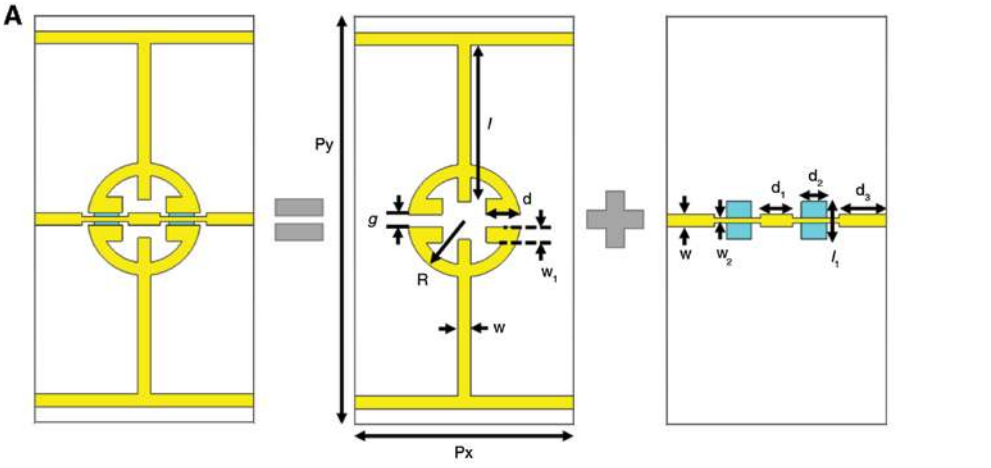

Px = 70 μm	Py = 180 μm	R = 18 μm
w = 4 μm	w_1 = 6 μm	w_2 = 1 μm
g = 4 μm	l = 76 μm	l_1 = 12 μm
d = 11 μm	d_1 = 10 μm	d_2 = 8 μm
d_3 = 15 μm		

Appendix-Figure 4: Simulation detail of LCDR: (A) 2D structure model, (B) structural parameters, and (C) transmission spectrum.

maximum resonance intensity. The field contour maps and transmission rates of these metaunits are also shown in these figures.

Appendix B: Details of the THz-TDS system and data processing

The THz-TDS, which is applied in the transmission experiment of this work, is produced by Teraview (TPS 3000) as shown in Appendix-Figure 5A. In the THz-TDS system, the THz transmitter and detector are laser gated photoconductive semiconductor devices. The femtosecond pulse generated by a Ti:sapphire ultrashort pulsed laser is split into two beams by a splitter: one beam is immediately received by detector and another beam, passing through an optical delay system, is focused onto a photoconductive antenna to generate THz radiation with a frequency range of 0.06–3 THz. A series of parabolic mirrors are set to make sure that THz beam is accurately focused on the sample and detector. All the measurements were performed in a superclean laboratory with 40% relative humidity. For instance, the time-domain data tested in air environment without sample are shown in Appendix-Figure 5B.

The reference phase is to the bare SiC substrate and the transmission is normalized by this substrate. The time-domain waveforms of the transmitted THz wave with different voltages are illustrated in Figure 8A. By performing a fast Fourier transformation of the time-domain waveform, the frequency-dependent amplitude $t(\omega)$ of the transmitted THz pulse through the metamaterial (Figure 8C) and frequency-dependent phase $p(\omega)$ (Figure 8B) are obtained. The bare SiC substrate is considered as the reference, which can be applied to normalize the electric field intensity and the phase spectra as below:

$$t(\omega) = E_{sample}(\omega) / E_{reference}(\omega)$$
$$p(\omega) = P_{sample}(\omega) - P_{reference}(\omega)$$

where $E_{sample/reference}(\omega)$ is the electric field intensity obtained from the time-domain data of the sample (reference) and $P_{sample/reference}(\omega)$ is the phase spectra of the sample (reference).

Appendix C: Test of C-V and I-V characteristics

We tested the I-V and C-V characteristics by Agilent B1500A and probe station (Appendix-Figure 6A). In addition to the above C-V curves (Figure 8E and F), we applied three probes to test the I-V characteristics of a single HEMT unit (Appendix-Figure 6B). As shown in Appendix-Figure 6C, the I-V curve illustrates that the performance of the single HEMT unit is very good and well electrically controlled.

Appendix D: 2DEG simulation model

According to the method presented in Ref. [17], we carried out the Drude model to characterize 2DEG with different carrier concentrations. To approximate the 2D charge density, we restricted the real part of the permittivity (ε_∞) to be equal to epsilon infinity ($9.7\varepsilon_0$ for GaN) and allowed the imaginary part to modeled by the Drude model. The complex relative permittivity can be expressed analytically as [17]

$$\varepsilon(\omega) = \varepsilon_\infty + i\omega_p^2 \frac{\gamma\omega^{-1}}{\omega^2 + \gamma^2}$$

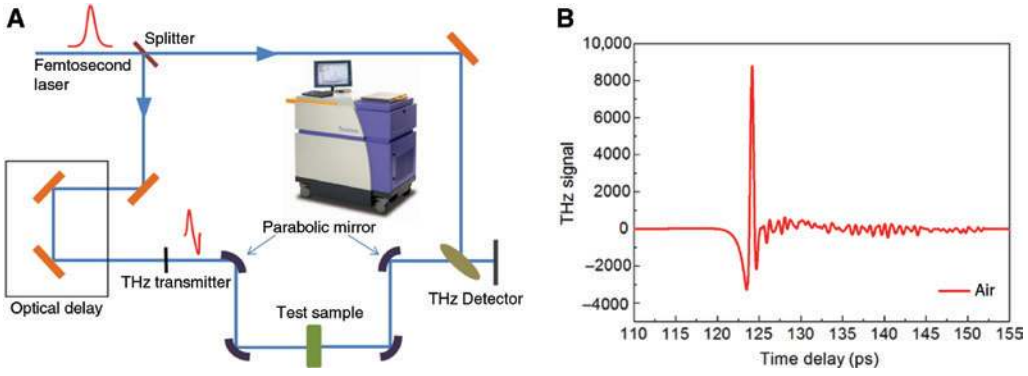

Appendix-Figure 5: THz-TDS experimental system: (A) THz-TDS in a transmission mode and (B) original time-domain data tested by this system.

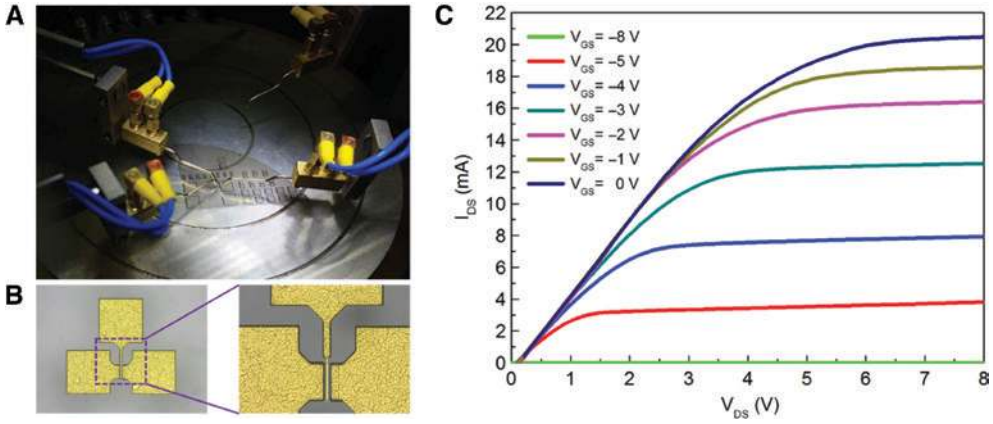

Appendix-Figure 6: (A) Probe experimental platform, (B) image of single HEMT, and (C) I-V curve for single HEMT.

In the imaginary part, $w_p{}^2 = e^2 N_S/\varepsilon_0 m^* d$ is the plasma frequency and the collision frequency $\gamma = 2\pi \times 1.4$ is calculated with the relation $\gamma = e/m^*\mu$, where μ is the electron mobility of the channel. e and m^* are the electron charge and effective mass in 2DEG, respectively. For the expression of plasma frequency, N_S is the 2D carrier concentration and d is the simulated model thickness of the channel layer.

In the simulation, when the plasma frequency is swept, the carrier concentration and the equivalent dielectric constant will change accordingly. The above methods enable an accurate modeling of this GaN-HEMT device in both the conductive (high 2DEG carrier concentration) and 2DEG-depleted states. This is representative of what occurs in experiments by applying a gate voltage of 0 V (conductive) and −8 V (depleted). Moreover, the continuous variation of the 2DEG carrier concentration with various DC biases is also shown.

Appendix E: Equivalent circuit model for LCDR

In this circuit model, due to the symmetry of the LCDR structure,

$$L_{21} = L_{22}$$
$$L_{31} = L_{32}$$
$$C_{31} = C_{32}$$
$$R_{21} = R_{22} = R_{31} = R_{32} = R_{23}$$

To get the transmission of the equivalent circuit model, we can use the equal impedance to simplify this model as

$$Z_{21} = R_{21} + j\omega L_{21}$$
$$Z_{22} = R_{22} + j\omega L_{22}$$
$$Z_{23} = R_{23} - j\frac{1}{\omega C_{23}}$$
$$Z_{31} = R_{31} - j\frac{1}{\omega C_{31}} + j\omega L_{31}$$
$$Z_{32} = R_{32} - j\frac{1}{\omega C_{32}} + j\omega L_{32}$$
$$Z_{21} = Z_{22} = Z_2$$
$$Z_{31} = Z_{32} = Z_3$$

The simplified equivalent circuit model is shown in Appendix-Figure 7. The input impedance of this equivalent circuit Z_{in} can be calculated using the following formula:

$$Z_{in} = \left\{\left[(j\omega L_1)//\left(-j\frac{1}{\omega C_0}\right)//\left(-j\frac{1}{\omega C_0}\right)//Z_{21}//Z_{22}\right] + \left[\left(-j\frac{1}{\omega C_1}\right)//Z_{23}\right]\right\}//Z_{31}//Z_{32}$$
$$= \left\{\left[(j\omega L_1)//\left(-j\frac{1}{\omega C_0}\right)//\left(-j\frac{1}{\omega C_0}\right)//Z_2//Z_2\right] + \left[\left(-j\frac{1}{\omega C_1}\right)//Z_{23}\right]\right\}//Z_3//Z_3$$
$$= \left\{\left[(j\omega L_1)//\left(-j\frac{1}{2\omega C_0}\right)//\frac{Z_2}{2}\right] + \left[\left(-j\frac{1}{\omega C_1}\right)//Z_{23}\right]\right\}//\frac{Z_3}{2}$$

$$
\begin{aligned}
&= \left[\left(\frac{j\omega L_1}{1-2\omega^2 L_1 C_0} // \frac{Z_2}{2}\right) + \left(\frac{-jZ_{23}}{-j+\omega C_1 Z_{23}}\right)\right] // \frac{Z_3}{2} \\
&= \frac{j\omega L_1 Z_2(-j+\omega C_1 Z_{23}) - jZ_{23}[2j\omega L_1 + Z_2(1-2\omega^2 L_1 C_0)]}{(-j+\omega C_1 Z_{23})[2j\omega L_1 + Z_2(1-2\omega^2 L_1 C_0)]} // \frac{Z_3}{2} \\
&= \frac{j\omega L_1 Z_2 Z_3(-j+\omega C_1 Z_{23}) - jZ_{23} Z_3[2j\omega L_1 + Z_2(1-2\omega^2 L_1 C_0)]}{2j\omega L_1 Z_2(-j+\omega C_1 Z_3) - 2jZ_{23} Z_3\{[2j\omega L_1 + Z_2(1-2\omega^2 L_1 C_0)] + (-j+\omega C_1 Z_{23})[2j\omega L_1 + Z_2(1-2\omega^2 L_1 C_0)]\}}
\end{aligned}
$$

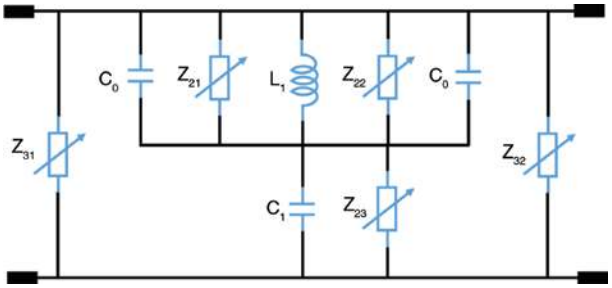

Appendix-Figure 7: Simplified equivalent circuit model for LCDR.

The values of the above parameters are shown in Appendix-Table 1. Then, the transmission can be calculated using the following formula:

$$T = \frac{2}{2 + jZ_{in}}$$

Appendix F: Relationship between phase and amplitude based on the KK relation

The KK relations connect the real and imaginary parts of a causal response function $G(t)$ used to describe the electromagnetic wave function. As we know, the electromagnetic wave function is just a frequency-domain response function, which is a complex relation as $G(\omega) = G'(\omega) + iG''(\omega)$, where $G'(\omega)$ and $G''(\omega)$ are the real and imaginary parts of the function.

The KK relations show the relationship between the real and imaginary parts of the frequency-domain response function as [58]

$$
\begin{aligned}
G'(\omega) &= \frac{2}{\pi} P\int_0^\infty \frac{\omega' G''(\omega')}{\omega'^2 - \omega^2} d\omega' \\
G''(\omega) &= -\frac{2\omega}{\pi} P\int_0^\infty \frac{G'(\omega')}{\omega'^2 - \omega^2} d\omega'
\end{aligned}
\tag{1}
$$

In Eq. (1), P denotes the Cauchy principal value.

It is known that the amplitude part and phase part of the frequency-domain response function of electromagnetic wave can be separated with Napierian logarithm as

$$\ln G(\omega) = \ln\left|G(\omega)\right| + i\angle G(\omega)$$

where $\angle G(\omega)$ is the phase part and $\ln|G(\omega)|$ is the amplitude part of the complex electromagnetic wave function $G(\omega)$. In Eq. (1), the expression of the relationship between phase and amplitude can be obtained:

$$\angle G(\omega) = -\frac{2\omega}{\pi} P\int_0^\infty \frac{\ln\left|G(\omega')\right|}{\omega'^2 - \omega^2} d\omega' \tag{2}$$

Next, the change variables have been applied:

$$v = \ln\left(\frac{\omega'}{\omega}\right), \quad \text{or } \omega' = \omega e^v, \text{ and } M(v) = \ln|G(\omega')|$$

where the range of the integration $v \to (-\infty, \infty)$, $d\omega' = \omega e^v dv$.

Expression (2) can be deduced to

$$
\begin{aligned}
\angle G(\omega) &= -\frac{2\omega}{\pi} P\int_{-\infty}^\infty \frac{M(v)}{\omega^2 e^{2v} - \omega^2} \omega e^v dv \\
&n - \frac{2}{\pi} P\int_{-\infty}^\infty \frac{M(v)}{e^{2v} - 1} e^v dv \\
&n - \frac{1}{\pi} P\int_{-\infty}^\infty \frac{M(v)}{\sinh v} dv
\end{aligned}
\tag{3}
$$

As the sinh is an odd function, only the odd part of $M(v)$ contributes in Eq. (3). $M(v)$ is the sum of odd and even function, $M(v) = M_o + M_e$. We have

Appendix-Table 1: Values of the parameters in equivalent circuit.

C_0	C_1	C_{31}, C_{32}	C_{23}	L_1	L_{21}, L_{22}	L_{31}, L_{32}	R_{21}, R_{22}, R_{31}, R_{32}, R_{23}
3.3fF	1.06pF	0.01fF	1.24pF	0.135pH	3.38pH	54nH	0.001 ~ 1900Ω

$$P\int_{-\infty}^{\infty}\frac{M(v)}{\sinh v}dv=\lim_{\varepsilon\to 0+}\left\{\int_{-\infty}^{-\varepsilon}+\int_{\varepsilon}^{\infty}\right\}\frac{M_o(v)+M_e(v)}{\sinh v}dv$$
$$=2\lim_{\varepsilon\to 0+}\int_{\varepsilon}^{\infty}\frac{M_o(v)}{\sinh v}dv \quad (4)$$

Next, considering the relation of $\int\frac{1}{\sinh v}dv=-\ln\coth\frac{v}{2}$ with integrating process, Eq. (4) becomes

$$P\int_{-\infty}^{\infty}\frac{M(v)}{\sinh v}dv=2\lim_{\varepsilon\to 0+}\left\{\int_{\varepsilon}^{\infty}\frac{dM_o}{dv}\ln\coth\frac{v}{2}dv-M_o\ln\coth\frac{v}{2}\Big|_{\varepsilon}^{\infty}\right\} \quad (5)$$

Next, considering the boundary terms vanishing [58]:

As $v\to\infty$, $\ln\coth\frac{v}{2}\sim 2e^{-v}=2\frac{\omega}{\omega'}$. As $\omega'\to\infty$, $|G(\omega')|$: ω'^{-n},

as physical response functions vanish at infinite frequencies. Then, $\ln|G(\omega')|$: $-n\ln\omega'$. Thus, $M_o\ln\coth\frac{v}{2}\sim\frac{\ln\omega'}{\omega'}\to 0$.

As $v\to 0$, $\ln\coth\frac{v}{2}\approx-\ln\frac{v}{2}$. As M_o is odd, $Mo\sim v+O(v^3)$. Thus, $v\ln v\to 0$.

Thus, Eq. (3) can be rewritten as

$$\angle G(\omega)=-\frac{2}{\pi}\int_0^{\infty}\frac{dM_o}{dv}\ln\coth\frac{v}{2}dv$$
$$=-\frac{1}{\pi}\int_{-\infty}^{\infty}\frac{dM}{dv}\ln\coth\frac{|v|}{2}dv \quad (6)$$

Finally, the phase function can be expressed as the relation of the derivation of the amplitude function as

$$\angle G(\omega)=\frac{\pi}{2}\int_{-\infty}^{\infty}\frac{dM_o}{dv}f(v)dv$$
$$f(v)=-\frac{2}{\pi^2}\ln\coth\frac{|v|}{2}$$
$$M(v)=\ln|G(\omega')| \quad (7)$$

Eq. (7) shows a very important relation:

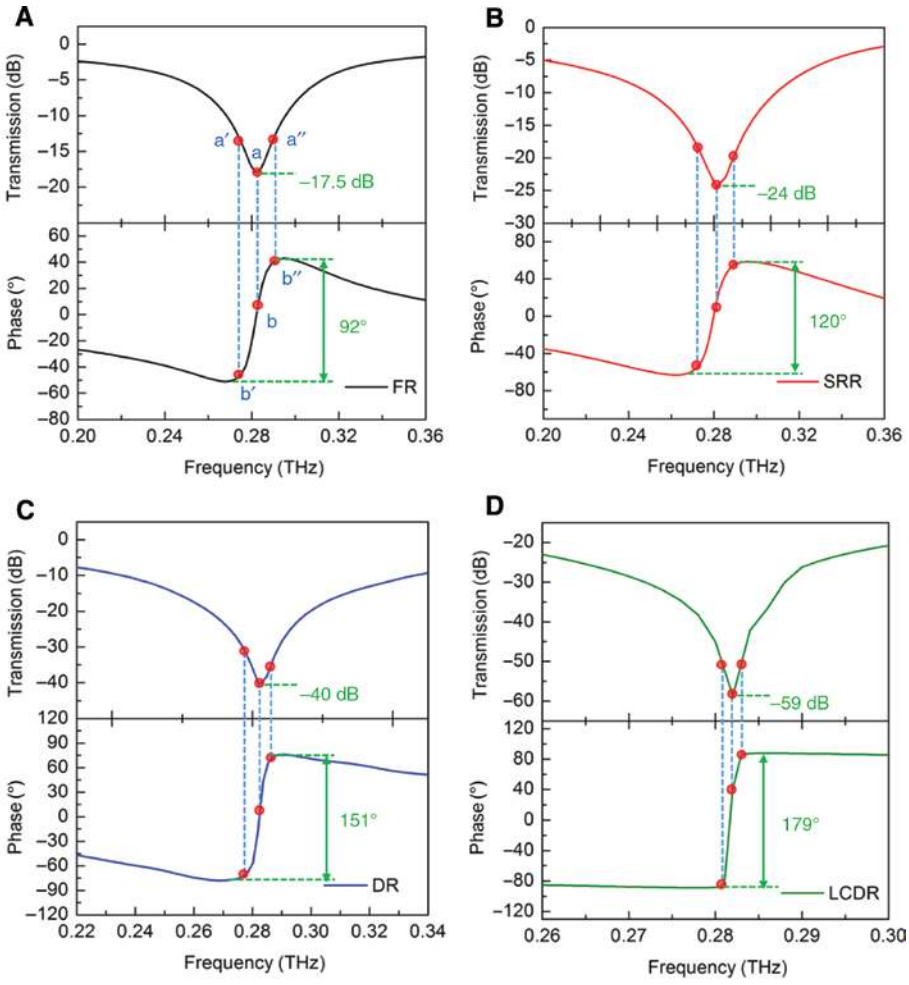

Appendix-Figure 8: Transmission and phase spectra for different structures: (A) FR, (B) SRR, (C) DR, and (D) LCDR.

Around the resonant frequency peak,

$$\nu \to 0,\ \omega \to \omega',\ \frac{dM}{d\nu} = \frac{d\ln|G|}{d\ln\omega},$$

so that the phase is positively correlated with the derivative of the amplitude function. Thus, based on this relation, it is clearly that the tip point of the resonant peak of the transmission amplitude is corresponding to the zero phase shown in Appendix-Figure 8. As shown in every simulation result, the largest phase b' and b'' (Appendix-Figure 8A) correspond to the largest $d\ln|G|/d\ln|\omega|$ (a' and a''), and the $\ln|G(\omega)|$ is just the amplitude function (the transmission function). Therefore, we can conclude the both the theoretical and simulation studies show that the phase is directly related to $d\ln|G|/d\ln|\omega|$. The value of the phase jump directly corresponds to the intensity of the resonant peak. The stronger resonant intensity could lead to the larger phase jump.

Acknowledgments: This work was supported by the National Natural Science Foundation of China (contract nos. 61270011, 91438118, 61741121, and 61501094, Funder Id: http://dx.doi.org/10.13039/501100001809), the National Key Basic Research Program of China (contract no. 2014CB339806), the Program for New Century Excellent Talents in University of Ministry of Education of China (grant no. NECT_13_0100), and the Sichuan Youth Science and Technology Foundation (no. 2014JQ0013).

Conflict of interest: The authors declare no competing financial interest.

References

[1] Siegel PH. Microw Theory Tech IEEE Trans 2002;50:910–28.
[2] Federici JF, Schulkin B, Huang F, et al. THz imaging and sensing for security applications – explosives, weapons and drugs. Semicond Sci Technol 2005;20:S266–80.
[3] Tonouchi M. Cutting-edge terahertz technology. Nat Photonics 2007;1:97–105.
[4] Zheludev NI, Kivshar YS. From metamaterials to metadevices. Nat Mater 2012;11:917–24.
[5] Liu AQ, Zhu WM, Tsai DP, Zheludev NI. Micromachined tunable metamaterials: a review. J Opt 2012;14:114009.
[6] Savinov V, Fedotov VA, Anlage SM, Groot PAJ, Zheludev NI. Modulating sub-THz radiation with current in superconducting metamaterial. Phys Rev Lett 2012;109:243904.
[7] Watts CM, Shrekenhamer D, Montoya J, et al. Terahertz compressive imaging with metamaterial spatial light modulators. Nat Photonics 2014;8:605–9.
[8] Mendis R, Nagai M, Wang YQ, Karl N, Mittleman MD. Terahertz artificial dielectric lens. Sci Rep 2016;6:23023.
[9] Mittleman DM. Frontiers in terahertz sources and plasmonics. Nat Photonics 2013;7:666–9.
[10] Reichel KS, Mendis R, Mittleman DM. A broadband terahertz waveguide T-junction variable power splitter. Sci Rep 2016;6:28925.
[11] Wang Q, Zhang XQ, Xu YH, et al. Broadband metasurface holograms: toward complete phase and amplitude engineering. Sci Rep 2016;6:32867.
[12] Chen HT, Padilla WJ, Zide JMO, Gossard AC, Taylor AJ, Averitt RD. Active terahertz metamaterial devices. Nature 2006;444:597–600.
[13] Shen NH, Massaouti M, Gokkavas M, et al. Optically implemented broadband blueshift switch in the terahertz regime. Phys Rev Lett 2011;106:037403.
[14] Shen XP, Cui TJ. Photoexcited broadband redshift switch and strength modulation of terahertz metamaterial absorber. J Opt 2012;14:114012.
[15] Kafesaki M, Shen NH, Tzortzakis S, Soukoulis CM. Optically switchable and tunable terahertz metamaterials through photoconductivity. J Opt 2012;14:114008.
[16] Chen HT, Padilla WJ, Cich MJ, Azad AK, Averitt RD, Taylor AJ. A metamaterial solid-state terahertz phase modulator. Nat Photonics 2009;3:148–51.
[17] Shrekenhamer D, Rout S, Strikwerda AC, et al. High speed terahertz modulation from metamaterials with embedded high electron mobility transistors. Opt Express 2011;19:9968–75.
[18] Driscoll T, Kim HT, Chae BG, et al. Memory metamaterials. Science 2009;325:1518–21.
[19] Jeong YG, Bernien H, Kyoung JS, et al. Electrical control of terahertz nano antennas on VO_2 thin film. Opt Express 2011;19:21211–5.
[20] Zhang YX, Qiao S, Sun H, Shi QW, Huang WX, Yang ZQ. Photoinduced active terahertz metamaterials with nanostructured vanadium dioxide film deposited by sol-gel method. Opt Express 2014;22:11070–8.
[21] Liu L, Kang L, Mayer TS, Werner DH. Hybrid metamaterials for electrically triggered multifunctional control. Nat Commun 2016;7:13236.
[22] Rodriguez BS, Yan R, Kelly MM, et al. Broadband graphene terahertz modulators enabled by intraband transitions. Nat Commun 2012;3:780.
[23] Lee SH, Choi M, Kim TT, et al. Switching terahertz waves with gate-controlled active graphene metamaterials. Nat Mater 2012;11:936–41.
[24] Rodriguez BS, Yan R, Rafique S, et al. Extraordinary control of terahertz beam reflectance in graphene electro-absorption modulators. Nano Lett 2012;12:4518–22.
[25] Liu M, Yin X, Avila EU, et al. A graphene-based broadband optical modulator. Nature 2011:1–4.
[26] Kindness SJ, Jessop DS, Wei B, et al. External amplitude and frequency modulation of a terahertz quantum cascade laser using metamaterial/graphene devices. Sci Rep 2017;7:7657.
[27] Gosciniak J, Tan DTH. Theoretical investigation of graphene-based photonic modulators. Sci Rep 2013;3:1897.
[28] Meng D, Wang S, Sun X, Gong R, Chen C. Actively bias-controlled metamaterial to mimic and modulate electromagnetically induced transparency. Appl Phys Lett 2014;104:261902.

[29] Li Q, Zhen T, Zhang XQ, et al. Active graphene-silicon hybrid diode for terahertz waves. Nat Commun 2015;6:7082.
[30] Yan R, Arezoomandan S, Berardi SR, Xing HG. Exceptional terahertz wave modulation in graphene enhanced by frequency selective surfaces. ACS Photonics 2016;3:315–23.
[31] Arezoomandan S, Yang K, Berardi SR. Graphene-based electrically reconfigurable deep-subwavelength metamaterials for active control of THz light propagation. Appl Phys A 2014;117:423–6.
[32] Yang K, Liu SC, Arezoomandan S, Nahata A, Berardi SR. Graphene-based tunable metamaterial terahertz filters. Appl Phys Lett 2014;105:093105.
[33] Hasan M, Arezoomandan S, Condori H, Berardi SR. Graphene terahertz devices for communications applications. Nano Commun Netw 2016;10:68–78.
[34] Urade Y, Nakata Y, Okimura K, et al. Dynamically Babinet-invertible metasurface: a capacitive-inductive reconfigurable filter for terahertz waves using vanadium-dioxide metal-insulator transition. Opt Express 2016;24:4405–10.
[35] Hashemi MRM, Yang SH, Wang TY, Nelson S, Mona J. Electronically-controlled beam steering through vanadium dioxide metasurfaces. Sci Rep 2016;6:35439.
[36] Lee SH, Choi M, Kim TT. Switching terahertz waves with gate-controlled active graphene metamaterials. Nat Mater 2012;11:936–41.
[37] Zhang YX, Qiao S, Liang SX. Gbps terahertz external modulator based on a composite metamaterial with a double-channel heterostructure. Nano Lett 2015;15:3501–6.
[38] Sun YF, Sun JD, Zhou Y, et al. Room temperature GaN/AlGaN self-mixing terahertz detector enhanced by resonant antennas. Appl Phys Lett 2011;98:252103.
[39] Scalari G, Maissen C, Turcinková D, et al. Ultrastrong coupling of the cyclotron transition of a 2D electron gas to a THz metamaterial. Science 2012;335:1323–6.
[40] Nouman MT, Kim HW, Woo JM, Hwang JH, Kim D, Jang J. Terahertz Modulator based on metamaterials integrated with metal-semiconductor-metal varactors. Sci Rep 2016;6:26452.
[41] Jackson JD. Classical Electrodynamics. 3rd ed. Hoboken, New Jersey, USA, John Wiley & Sons, 1998.
[42] Sara A, Berardi SR. Geometrical tradeoffs in graphene-based deeply-scaled electrically reconfigurable metasurfaces. Sci Rep 2015;5:8834.
[43] Papasimakis N, Fu YH, Fedotov VA, Prosvirnin SL, Tsai DP, Zheludev NI. Metamaterial with polarization and direction insensitive resonant transmission response mimicking electromagnetically induced transparency. Appl Phys Lett 2009;94:211902.
[44] Boris LY, Zheludev N, Stefan M, et al. The Fano resonance in plasmonic nanostructures and metamaterials. Nat Mater 2010;9:707–15.
[45] Zhang SP, Bao K, Halas NJ, Xu HX, Peter N. Substrate-induced Fano resonances of a plasmonic nanocube: a route to increased-sensitivity localized surface plasmon resonance sensors revealed. Nano Lett 2011;11:1657–63.
[46] Singh R, Ibraheem AN, Yang YP, et al. Electromagnetically induced transparency in an individual Fano resonator metamaterial. CLEO Techn Dig 2012;1509:1.
[47] Chiam SY, Singh R, Rockstuhl C, Falk L, Zhang WL, Andrew AB. Analogue of electromagnetically induced transparency in a terahertz metamaterial. Phys Rev B 2009;80:153103.
[48] Liu N, Langguth L, Thomas W, et al. Plasmonic analogue of electromagnetically induced transparency at the Drude damping limit. Nat Mater 2009;8:758–62.
[49] Worawut K, Jens D, Moritz E, et al. Quantitative and direct near-field analysis of plasmonic-induced transparency and the observation of a plasmonic breathing mode. ACS Nano 2016;10:2214–24.
[50] Gu JQ, Singh R, Liu XJ, et al. Active control of electromagnetically induced transparency analogue in terahertz metamaterials. Nat Commun 2012;3:1151.
[51] Xu Q, Zhang XQ, Xu YH, et al. Plasmonic metalens based on coupled resonators for focusing of surface plasmons. Sci Rep 2016;6:37861.
[52] Liu XJ, Gu JQ, Singh R, et al. Electromagnetically induced transparency in terahertz plasmonic metamaterials via dual excitation pathways of the dark mode. Appl Phys Lett 2012;100:131101.
[53] Imogen MP, Yousif AK, Koray A, Harry AA. Compliant metamaterials for resonantly enhanced infrared absorption spectroscopy and refractive index sensing. ACS Nano 2011;5:8167–74.
[54] Yosuke N, Yoshiro U, Kunio O, et al. Anisotropic Babinet-invertible metasurfaces to realize transmission-reflection switching for orthogonal polarizations of light. Phys Rev Lett 2016;6:044022.
[55] Yoshiro U, Yosuke N, Toshihiro N, Masao K. Frequency-independent response of self-complementary checkerboard screens. Phys Rev Lett 2015;114:237401.
[56] Yoshiro U, Yosuke N, Toshihiro N, Masao K. Broadband and energy-concentrating terahertz coherent perfect absorber based on a selfcomplementary metasurface. Opt Lett 2016;41:19.
[57] Sara A, Hugo OCQ, Nicholas R, Cesar AN, Berardi SR. Graphene-based reconfigurable terahertz plasmonics and metamaterials. Carbon 2017;112:177–84.
[58] Bechhoefer J. Kramers-Kronig, Bode, and the meaning of zero. Am J Phys 2011;79:1053–9.